



Clumped fluoride-hydroxyl defects in forsterite:Implications for the upper-mantle

Céline Crépisson, Marc Blanchard, Hélène Bureau, Chrystèle Sanloup,
Anthony C. Withers, Hicham Khodja, Suzy Surblé, Caroline Raepsaet, Keevin
Béneut, Clémence Leroy, et al.

► To cite this version:

Céline Crépisson, Marc Blanchard, Hélène Bureau, Chrystèle Sanloup, Anthony C. Withers, et al..
Clumped fluoride-hydroxyl defects in forsterite:Implications for the upper-mantle. *Earth and Plane-
tary Science Letters*, 2014, 390, pp.287-295. 10.1016/j.epsl.2014.01.020 . hal-00959948

HAL Id: hal-00959948

<https://hal.science/hal-00959948>

Submitted on 17 Mar 2014

HAL is a multi-disciplinary open access archive for the deposit and dissemination of scientific research documents, whether they are published or not. The documents may come from teaching and research institutions in France or abroad, or from public or private research centers.

L'archive ouverte pluridisciplinaire **HAL**, est destinée au dépôt et à la diffusion de documents scientifiques de niveau recherche, publiés ou non, émanant des établissements d'enseignement et de recherche français ou étrangers, des laboratoires publics ou privés.

Title: Clumped fluoride-hydroxyl defects in forsterite:

Implications for the upper-mantle

Authors: Céline Crépisson¹, Marc Blanchard^{1*}, Hélène Bureau¹, Chrystèle Sanloup^{2,3},
Antony C. Withers⁴, Hicham Khodja⁵, Suzy Surblé⁵, C. Raepsaet⁵, Keevin Béneut¹, Clémence
Leroy¹, Paola Giura¹, Etienne Balan¹

¹ Institut de Minéralogie et Physique des Milieux Condensés (IMPMC) UMR CNRS 7590,
UMR IRD 206, Université Paris VI, case 115, 4 place Jussieu, 75252 Paris cedex 05, France

² SUPA, Centre for Science at Extreme Conditions and School of Physics and Astronomy,
University of Edinburgh, Edinburgh EH9 3JZ, UK

³ Institut des Sciences de la Terre de Paris (ISTEP) UMR CNRS 7193, Université Paris VI, 4
place Jussieu, 75252 Paris, cedex 05 France

⁴ Department of Earth Sciences, Western University, London, ON, Canada

⁵ CEA/DSM/IRAMIS/SIS2M, UMR3299, CEA Saclay, 91191 Gif sur Yvette, France

*Corresponding author. *E-mail address:* marc.blanchard@impmc.upmc.fr ; *Tel.:* +33 1 44279822 ;
fax: +33 1 44273785

Keywords fluorine, olivine, infrared spectroscopy, *ab initio* calculations, DFT, OH defects,
Ion Beam Analysis

Abstract

The mechanism and magnitude of fluorine incorporation in H-bearing forsterite were investigated through a combined experimental and theoretical approach. Forsterite samples were synthesized in a piston cylinder press at 2 and 4 GPa, in hydrous conditions, with or without fluorine. High fluorine solubilities of 1715 and 1308 ppm F were measured by particle induced gamma-ray emission (PIGE) in forsterites synthesized at 2 and 4 GPa, respectively. In addition, first-principles calculations based on density functional theory were performed in order to investigate the coupled incorporation mechanisms of fluorine and water in forsterite. Our results demonstrate the close association of fluoride, hydroxyl groups and Si vacancies. Comparison of experimental and theoretical infrared absorption spectra enables assignment of the nine OH stretching bands ($3500\text{-}3700\text{ cm}^{-1}$) observed in F-rich synthetic forsterite to clumped fluoride-hydroxyl defects in the forsterite crystal structure. Noteworthy, similar bands were previously recorded on some natural olivine with $\text{Mg}/(\text{Mg}+\text{Fe})$ molar ratio down to 0.86. Fluorine and water cycles are therefore strongly coupled through the nominally anhydrous minerals and the mantle fluorine budget can be entirely accommodated by these mineral phases.

41 **1. Introduction**

42 Very little is known about the deep fluorine cycle. The presence of fluorine in volcanic
43 gases and melt inclusions shows that there is a fluorine flux from the depth to the surface
44 (Schilling et al., 1980; Aoki et al., 1981; Symonds et al., 1988; Bureau et al., 1998; Pyle and
45 Mathers, 2009). Fluxes from surface to depth are also expected at subduction zones, where
46 serpentinites are the most likely carrier of halogen elements including fluorine (John et al.,
47 2011 and references therein). Fluorine released from the dehydration of the oceanic crust can
48 be degassed during through arc volcanism or may be recycled back into the mantle with an
49 efficiency of around 95% (Straub and Layne, 2003; John et al., 2011). Significant fluorine
50 enrichments in mantle rocks are suggested by elevated concentrations (0.2 wt%) in some
51 kimberlite samples (Paul et al., 1975) and by the identification of "fluoride melts" in a
52 metasomatized mantle xenolith from New Zealand (Klemme, 2004). Estimates of the fluorine
53 concentration of the primitive Earth mantle based on CI carbonaceous chondrite range from
54 15 ppm to 25 ppm (McDonough and Sun, 1995; Palme and Jones, 2003).

55 Little is also known about fluorine incorporation in the solid Earth. For long it has
56 been proposed that the main fluorine carriers were hydrous and minor accessory minerals
57 such as apatite, micas, amphibole (Smith et al., 1981; Smith, 1981) or clinohumite (Brey et
58 al., 2009). The role of nominally anhydrous and fluorine-free silicates as a deep fluorine
59 reservoir has only recently been proposed (Hervig and Bell, 2005; Bromiley and Kohn, 2007;
60 Beyer et al., 2012; Dalou et al., 2012; Bernini et al., 2013; Mosenfelder and Rossman, 2013a,
61 2013b; Fabbrizio et al., 2013). In particular, fluorine solubility in olivine, the main constituent
62 of the upper mantle, could reach 900 ppm (Fabbrizio et al., 2013), 1900 ppm (Bernini et al.,
63 2013) or even 4500 ppm (Bromiley and Kohn, 2007). The incorporation mechanism of
64 fluorine in these nominally anhydrous and fluorine-free silicates remains speculative. Crystal-

chemical considerations based on the similar ionic radius of fluoride (0.130 nm) and hydroxyl ions (0.136 nm) suggest that fluoride incorporation could share some similarities with the incorporation of OH groups in these minerals. As a matter of fact, the fluoride for hydroxyl substitution is commonly observed in hydrous minerals (e.g. amphibole, Robert et al., 1999). The substitution has also been reported in some nominally anhydrous silicates, such as garnet (Visser, 1993) and zircon (Caruba et al., 1985; Balan et al., 2013), and in high pressure hydrous phases, such as superhydrous phase B (Hazen et al., 1997).

In the present study, we determine the mechanism and magnitude of fluorine incorporation in H-bearing forsterite (Fo100) by experiment and theory. This work is completed by the further investigation (Particle Induced Gamma-ray Emission measurements PIGE) of the synthetic samples from Withers et al. (2011, 2012), which have a composition similar to mantle olivine (Fo90). The results demonstrate the close association of fluoride, hydroxyl groups and Si vacancies. Implications for fluorine storage in the upper mantle are discussed.

2. Materials and Methods

2.1. Syntheses and preparation

Forsterite samples were synthesized in a piston cylinder press at the University of Edinburgh, CSEC. The starting material was prepared by homogenizing a mixture of high purity (reagent grade) reactants (MgO, SiO₂, Mg(OH)₂, and NaF). The Mg/Si molar ratio of the starting material was 1.75, initial H₂O and F contents were ~5 and ~1.1 wt%, respectively. Experiments were performed at 2 GPa (run #PC36F) and 4 GPa (run #PC38 and #PC38F), at ~ 1250°C, in a 3 cm long cell-assembly composed of a graphite heater surrounded by pyrex and talc sleeves. Two welded 5 mm height and 3 mm outer diameter Au₇₅Pd₂₅ capsules, with and without NaF, were simultaneously inserted in the press on top of each other and separated

by an alumina disk. MgO powder dried overnight at 1000C was packed around the Au₇₅Pd₂₅ capsules. Experiments were run for 3 days and terminated by turning-off the heater before a slow decompression. Temperature was monitored with a Type C thermocouple (W₇₄Re₂₆-W₉₅Re₅) whose extremity was in contact with the top capsule.

2.2. Electron microscopy and microprobe analysis

Forsterite grains were mounted on a metallic disk with carbon tape and coated with a 10 nm thick carbon film. The texture of the samples was examined with a Zeiss Ultra 55 field emission scanning electron microscope (SEM) with a working distance of 3±0.2 mm and an acceleration voltage of 15 keV. Major elements were analyzed using a Cameca SX FIVE electron microprobe at CAMPARIS facility (UPMC). Acceleration voltage was set to 15 keV, current to 10 nA and beam was focused to 10 µm diameter at the surface of the sample. Counting times were 10 s both on the sample and the background.

2.3. Vibrational spectroscopy

IR measurements were done on a Bruker IFS 66v/S Fourier transform infrared spectrometer working in vacuum and aligned in transmission geometry. The sample was disposed in a homemade sample chamber at the focal point of two cassegrainian reflectors. The analysis area of the sample was selected with slits located between the sample and the detector. Every spectrum was acquired in the frequency region 550-9000 cm⁻¹ with resolution of 4 cm⁻¹ and accumulation of 64 scans using the mid infrared instrumental configuration i.e. Globar, KBr and MCT as respectively source, beam splitter and detector. The background was measured after each sample measurement without changing analysis conditions. Absorbance was obtained after subtraction of the baseline using the OPUS/IR software. Seven to ten grains (50 to 150 µm thick) from each capsule were analyzed. After normalization to

thickness and subtraction of epoxy signal and baseline, average unpolarized absorption spectra were calculated and fit using Lorentzian line-shapes (Table 1). In the wavenumber range of interest, the epoxy signal corresponds to a strong band at $\sim 3440\text{ cm}^{-1}$, where there is no olivine OH band, plus a weak and broad band centred at $\sim 3550\text{ cm}^{-1}$. The epoxy correction was made for two of the seven spectra of the PC38 synthesis and three of the ten spectra of the PC36F synthesis.

Raman spectroscopic measurements were performed with a Renishaw InVia Raman spectrometer coupled with an optical microscope, using a 514.5 nm laser excitation radiation (1 mW power) and a 1200 mm^{-1} grating. Spectra were acquired from 100 to 2200 cm^{-1} , and averaged from 4 accumulations, each with a counting time of 60 s.

2.4. Ion beam analysis

Particle induced gamma ray emission (PIGE), Rutherford backscattering spectrometry (RBS) and Elastic Recoil Detection Analysis (ERDA) were performed at the nuclear microprobe of CEA Saclay SIS2M / LEEL (Khodja et al., 2001). In both cases particle induced X-ray emission (PIXE) and Rutherford Backscattering RBS measurements were simultaneously associated to PIGE and ERDA. PIGE is based on the detection of γ -ray emission during a nuclear reaction triggered by a high-energy proton beam and makes it possible to determine accurately fluorine concentrations. The γ -ray emission at 109.9 keV of the $^{19}\text{F}(\text{p},\text{p}'\gamma)$ nuclear reaction induced by a 3 MeV proton beam was detected with an HP-Ge detector (Mosbah et al., 1991). ERDA is based on the detection of protons at a low ‘grazing’ angle of 15° from a ^4He incident beam of 3 MeV after they have been ejected from the samples through elastic collisions, this method has been recently used to quantify water in nominally anhydrous minerals; details about the procedure are described in (Raepsaet et al., 2008; Bureau et al., 2009, Withers et al., 2012). PIXE and RBS measurements allow chemical

characterization of the sample with respect to major and trace elements. RBS measurements were performed using an annular detector positioned at 170° with respect to the incident beam direction, in order to monitor the electrostatic charge delivered to the sample. Further details can be found in Bureau et al. (2009) and Habrioux et al. (2012). All analyses were performed by scanning a 4 μm × 4 μm microbeam on 100 μm × 100 μm areas.

In PIGE analysis, the fluorine concentration is determined by comparison with a reference sample using the following relation:

$$\frac{[X_{sample}]}{[X_{std}]} = \frac{S_{sample}}{S_{std}} \times \frac{A_{sample}}{A_{std}} \times \frac{N_{\omega_{std}}}{N_{\omega_{sample}}} \quad (1)$$

where A is the peak area associated with γ -ray transitions observed for element X , S the stopping power of the sample and N_{ω} the number of protons by solid angle unit delivered to the selected area. The reference sample was a pantellerite glass with F content of 4200 ppm and a similar stopping power to the forsterite samples (KE12; Métrich and Rutherford, 1991). Calibration was verified on a Macusanite glass with known F content of 1.33 wt% determined by EMPA (Pichavant et al., 1987). Data were processed with the RISMIN software (Daudin et al., 2003) following the procedure described in Bureau et al. (2009). Statistical errors are around 10%. A fit of the RBS spectra with the SIMNRA software (Mayer, 1997), using the olivine matrix composition, enables determination the N_{ω} parameters.

2.5. Theoretical methods

Calculations were performed using the theoretical approach and convergence parameters described in Balan et al. (2011). Calculations are based on the density functional theory, with the generalized gradient approximation (GGA) to the exchange-correlation functional as proposed by Perdew, Burke and Ernzerhof (Perdew et al., 1996) and periodic boundary conditions. Structure relaxations were done on a 2×1×2 supercell (112 atoms) of

forsterite using the PWscf code of the Quantum Espresso package (Giannozzi et al., 2009; <http://www.quantum-espresso.org>). The theoretical relaxed primitive orthorhombic-cell parameters of anhydrous forsterite are $a = 4.78 \text{ \AA}$, $b = 10.28 \text{ \AA}$, and $c = 6.01 \text{ \AA}$ ($Pbnm$ space group). The optimized cell parameters of pure forsterite were kept constant during the relaxation of the F- and OH-bearing supercells. During this step, no symmetry constraint was applied to the atomic positions and the forces on atoms were minimized to less than 10^{-4} Ry/a.u. Following the same procedure as Balan et al. (2011) high-frequency OH stretching modes and corresponding IR absorption spectra were calculated from the dynamical matrix, Born effective charge tensors and dielectric tensor, obtained using the density functional perturbation theory (Baroni et al., 2001) as implemented in the Phonon code of the Quantum Espresso package (Giannozzi et al., 2009; <http://www.quantum-espresso.org>).

3. Results

3.1. *Chemical composition and infrared spectra of synthetic forsterite samples*

The investigated samples consist of transparent and large ($> 100 \text{ }\mu\text{m}$) forsterite crystals with no observed inclusions (Fig. 1). Coexisting enstatite crystals are also identified at the top of the capsule by Raman measurements. Major element analyses indicate that the forsterite grains are close to the stoichiometric composition (Table 1). Beside OH defects, the major measured impurity is fluorine. Concentrations of 1715 ppm F and 1308 ppm F are measured by PIGE at 2 GPa (PC36F) and 4 GPa (PC38F) respectively (Table 1). Minor Na concentrations are also detected by PIGE, i.e. 131 ppm Na and 81 ppm Na at 2 GPa (PC36F) and 4 GPa (PC38F) respectively. These Na concentrations do not exceed the typical range of few hundreds of ppm expected for Na in olivine (e.g. Borisov et al., 2008).

The OH-stretching infrared absorption spectrum of the F-free forsterite sample (#PC38, Fig. 2) is similar to that reported in previous studies (Lemaire et al., 2004; Bali et al.,

2008; Ingrin et al., 2013). It is dominated by the "hydrogarnet-type" defect $(4\text{H})^{\text{x}}_{\text{Si}}$ responsible for a cluster of narrow absorption bands in the $3620\text{--}3550\text{ cm}^{-1}$ region (Balan et al., 2011; Umemoto et al., 2011). Two broader bands observed in the same region have been recently attributed to interstitial OH-groups (Ingrin et al., 2013; Balan et al., 2013). Weak and broad bands ascribed to protonated Mg vacancies (e.g. Balan et al., 2011) are observed at 3160 and 3220 cm^{-1} ; whereas weak and narrow bands observed between 3300 and 3400 cm^{-1} could be related to trace amounts of trivalent impurities (Berry et al., 2007).

The OH-stretching spectra of F-bearing forsterite samples (#PC36F and #PC38F) are similar to each other. They are also similar to the unpolarized spectrum of a F-rich forsterite (900 ppm F) synthesized at 1200°C and 2 GPa by Fabbrizio et al. (2013). Although still dominated by a group of intense bands observed in the $3700\text{--}3500\text{ cm}^{-1}$ region, they differ significantly from that of the F-free sample (#PC38). These bands are not observed in F-free forsterite and are rarely seen in natural samples. The most intense band is located at 3570 cm^{-1} with a shoulder at 3555 cm^{-1} . Seven other intense bands occur at 3674 , 3641 , 3624 , 3597 , 3591 , 3535 and 3514 cm^{-1} (Table 1). The 3612 cm^{-1} band related to $(4\text{H})^{\text{x}}_{\text{Si}}$ is still visible but very weak (Fig. 2). Small variations in the relative intensities of the F-related bands in #PC36F and #PC38F cannot be considered as significant owing to the limited number of measurements used to build average IR spectra (Fig. 3). Some bands observed here are close in frequency to OH bands reported previously in natural olivine samples and assigned to hydrous nano-inclusions, such as talc, serpentine or Ti-clinohumite (Beran and Libowitzky, 2006). Among the defects related to Ti-clinohumite, Ti planar defects give rise to a band at 3410 cm^{-1} and the Ti point defect leads to two bands at 3572 and 3525 cm^{-1} (Berry et al., 2005; Balan et al., 2011). In the present spectra (Fig. 2), no bands are observed at 3525 and 3410 cm^{-1} , which would suggest the absence of Ti related defects. Furthermore, no significant presence of Ti has been detected by PIXE during the ERDA analysis of the samples. Talc

corresponds to an OH band at 3677 cm^{-1} and bands in the range $3640\text{--}3700\text{ cm}^{-1}$ can be referred to serpentine (Beran and Libowitzky, 2006). The two highest bands, observed here at 3674 and 3641 cm^{-1} , could then be assigned to talc or serpentine nano-inclusions that would be nearly homogeneously distributed in all crystals sampled from the two experiments but as it will be shown further by the calculations, intrinsic hydroxylated point defects in the crystal structure of F-bearing forsterite can already explain these bands. The significant modifications observed between the F-free and the F-bearing forsterite samples thus suggest that fluoride ions are associated with these OH-bearing defects.

Interestingly, the infrared spectrum of the F-rich synthetic forsterite samples is nearly identical to that of a natural F-rich forsterite sample from Pamir, Tadjikistan (Libowitzky and Beran, 1995), here referred to as the Pamir olivine (Fig. 4a). All the bands observed in the synthetic samples are present in the Pamir sample, except a shoulder at 3555 cm^{-1} and the small band at 3612 cm^{-1} related to $(4\text{H})_{\text{Si}}^{\text{x}}$ defects. Noteworthy, other natural olivine samples described in the literature display absorption bands at wavenumbers close to those reported here for the F-bearing synthetic samples (Sykes et al., 1994; Kishina et al., 2001; Bell et al., 2004, Matsyuk and Langer, 2004; Koch-Müller et al., 2006, Mosenfelder et al., 2011). For these natural samples, Mosenfelder et al. (2011) specifically attributed the three bands above 3600 cm^{-1} to coupled substitutions of hydroxyl and fluoride.

Water contents are 448 ± 90 ppm H_2O in F-free forsterite; 267 ± 53 ppm H_2O and 887 ± 124 ppm H_2O in F-rich forsterite samples synthesized at 4 and 2 GPa, respectively (Table 1). As a comparison, Lemaire et al. (2004) measured water contents ranging from 42 to 750 ppm in synthetic forsterite synthesized at 2 GPa and Withers et al. (2012) measured a water content of 462 ppm in olivine ($\text{Mg}\# = 90$) synthesized at 3 GPa.

Water and fluorine contents are higher for forsterite synthesized at 2 GPa (#PC36F) than at 4 GPa (#PC38F), however a tendency can hardly be defined with only two pressures

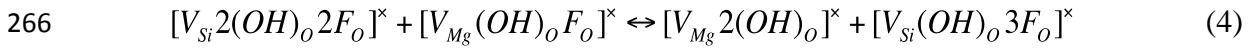
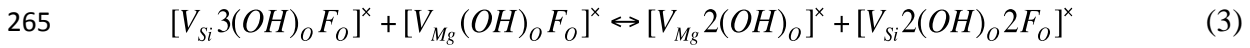
investigated. Further experiments are needed to define the effect of pressure on simultaneous water and fluorine incorporation in olivine.

3.2. Theoretical results

Infrared spectroscopic measurements suggest that fluoride ions are associated with OH defects in the structure of F-bearing forsterite. Starting from the models of $(4\text{H})^{\text{x}}_{\text{Si}}$ and $(2\text{H})^{\text{x}}_{\text{Mg}}$ defects previously determined by Balan et al. (2011), the structure of fluorinated defects was obtained by substituting fluoride ions for OH groups. The most stable configurations of clumped fluoride and OH defects associated with Si vacancies are displayed in Fig. 4.a. For a single F-for-OH substitution, three configurations of almost equal stability (within 2 kJ.mol^{-1}) are obtained, denoted as $\text{F}_{(\text{O}1)}$, $\text{F}_{(\text{O}2)}$ and $\text{F}_{(\text{O}3)}$ for F in O1, O2 and O3 site, respectively. Other orientations of OH groups lead to significantly less stable configurations (by $\sim 30 \text{ kJ.mol}^{-1}$). When two F for OH substitutions are considered, two configurations are found equally stable (within 1.1 kJ.mol^{-1}): $2\text{F}_{(\text{O}2, \text{O}1)}$ and $2\text{F}_{(\text{O}2, \text{O}3)}$ corresponding respectively to OH/F substitutions in O2 and O1 sites and to OH/F substitutions in O2 and O3 sites. For three F for OH substitutions, the most stable configuration is obtained for F ions located in O2 and in the two symmetrical O3 sites ($3\text{F}_{(\text{O}3, \text{O}3, \text{O}2)}$) with the OH group pointing toward the center of the vacancy.

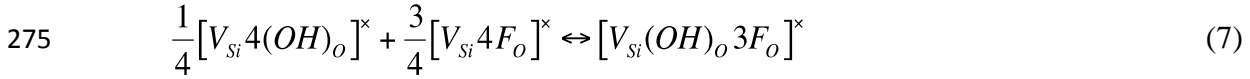
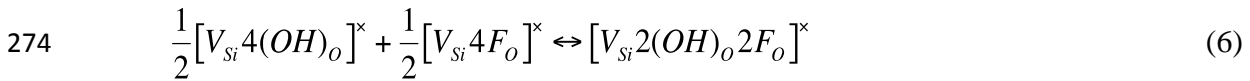
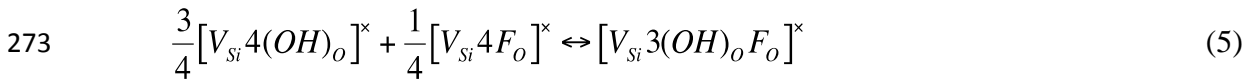
For a Mg vacancy, the most stable configuration corresponds to a F substituting for the OH at the O2 site. The position of the remaining OH group in O2 site is almost unchanged. Its OH bond length is slightly shortened (1.000 \AA versus 1.003 \AA in the fully protonated Mg vacancy).

Assuming that both Mg and Si vacancies are present in the crystal, the preferential fluorination of Mg or Si vacant sites can be described by three reactions, depending on the number of fluoride ions considered:



The total energy difference associated with these three reactions is always significantly negative (-101 kJ.mol⁻¹, -98 kJ.mol⁻¹ and -81 kJ.mol⁻¹ for reactions 2, 3 and 4, respectively). This suggests that OH/F substitutions are more likely to occur in Si protonated vacancies than in Mg protonated vacancies.

Similarly, the relative stability of mixed OH/F defects associated to Si vacancies can be compared to that of equivalent proportions of pure F and OH defects:



The total energy difference associated with these reactions is always significantly negative (-19 kJ.mol⁻¹, -34 kJ.mol⁻¹ and -32 kJ.mol⁻¹ for reactions 5, 6 and 7 respectively). Although the absolute abundance of mixed OH/F defects also depends on the fluorine activity and H₂O fugacity, the greater stability of mixed OH/F defects with respect to the defect end-members is consistent with the weakness of the signal ascribed to fully protonated Si vacancies.

The theoretical IR absorption spectrum corresponding to the OH-stretching modes of the seven most stable geometries of the OH- and F-bearing defects associated with Mg and Si vacancies have been computed.

In the case of an Mg vacancy, one OH/F substitution induces an upshift of the band from 3222 to 3291 cm⁻¹, compared to the fully protonated Mg vacancy, while the polarization

along the z axis remains unchanged (Balan et al., 2011). This frequency shift is directly related to the geometrical changes related to the presence of the fluoride ion.

The IR spectra generated for the six most stable configurations of OH/F defects in Si site are displayed in Fig. 4. For one OH/F substitution, each of the three configurations ($F_{(O1)}$, $F_{(O2)}$ and $F_{(O3)}$) lead to three distinct bands (Fig. 4b). The most intense is strongly polarized along x (respectively at 3611, 3583 and 3556 cm^{-1}) whereas the two other bands at lower frequency are polarized along y and z (respectively around 3577, 3534 and 3505 cm^{-1} , with a splitting smaller than 10 cm^{-1}). Most of the bands result from a coupling between 2 or 3 OH-groups of the defects. OH-bands related to two OH/F substitutions fall very close to contributions from the 1 OH/F substitution (Fig. 3c). Configuration $2F_{(O2, O1)}$ leads to one band strongly polarized along x (3581 cm^{-1}) and one band polarized along z (3554 cm^{-1}) whereas configuration $2F_{(O2, O3)}$ leads to one band strongly polarized along x (3610 cm^{-1}) and one band polarized equally along x and z (3546 cm^{-1}). All absorption bands arise from coupled vibrational motions of the two OH groups. Finally, $3F_{(O3, O3, O2)}$ is associated with one band at higher frequency (3674 cm^{-1}) strongly polarized along x (Fig. 4d).

Lack of polarized measurement prevents a thorough comparison of the theoretical IR spectra with the spectrum of the present synthetic F-rich forsterite. However, the 3700-3500 cm^{-1} region of the average IR spectrum of the synthetic samples is very similar to the spectrum of the Pamir olivine (Fig. 5a). We thus consider that the theoretical IR spectra can be compared with the polarized spectrum of the Pamir olivine reported on Fig. 5 (Libowitzky and Beran, 1995). We point out that different polarizations for what seems to be single experimental bands on the Pamir olivine spectrum are often explained by theoretically calculated contributions from different defects.

The band at 3674 cm^{-1} (band a, Fig. 5) is well explained by the configuration $3F_{(O3, O3, O2)}$ which shows a band strongly polarized along x at the same wavenumber. Although the two

theoretical frequencies almost coincide at 3610-3611 cm^{-1} , the bands at 3641 and 3624 cm^{-1} (bands b and b') are best explained by the $2F_{(O2, O3)}$ and $F_{(O1)}$ defects, with the main polarization along x and a much smaller polarization along z. The weakly split bands around 3597 and 3591 cm^{-1} (bands c and c') can be attributed to contributions from the configurations $2F_{(O1, O2)}$ and $F_{(O2)}$ for the x component and from configuration $F_{(O1)}$ for the weaker z and y components. The intense band at 3570 cm^{-1} (band d) is well reproduced by configuration $F_{(O3)}$ giving a band at 3556 cm^{-1} with a polarization along x, whereas the contribution along z could arise from the $2F_{(O1, O2)}$ defect. Finally, the band e at 3535 cm^{-1} could be related to the configuration $F_{(O3)}$. However, the polarization properties, relative intensity and band positions of the experimental band e are not well reproduced and this assignment is still very speculative. Furthermore, there are differences between the spectrum of the synthetic forsterite and that of the Pamir olivine with the presence of a band at 3515 cm^{-1} (Fig. 5): the band e could actually turn into a doublet reproduced by the configuration $F_{(O3)}$ though polarization remains unexplained.

3.3. Integrated molar absorption coefficients of OH defects in forsterite

For each configuration we calculate the integrated molar absorption coefficients for F- and OH-bearing defects. Results are given in Figs. 4b, 4c and 4d for F-bearing Si vacancies and we find a value of 135668 cm^{-2} per mol $\text{H}_2\text{O/L}$ for an Mg defect with one OH/F substitution. These new data are aligned along a similar trend to OH defects in F-free forsterite (Fig. 6), i.e. on a line rather parallel to the general trend from Balan et al. (2008) but with a downward offset of $\sim 50000 \text{ cm}^{-2}$ per mol $\text{H}_2\text{O/L}$. This shift is consistent with previous findings on F-free forsterite by Balan et al. (2011). Therefore, the molar absorption coefficient derived from F-free olivine by Withers et al. (2012) can also be applied to F-rich olivine. Noteworthy, the $3F_{(O3, O3, O2)}$ defect is not on the same trend as the other defects. Despite a

higher frequency, its molar absorption coefficient is close to values obtained for the other defects. This suggests that all Si defects in forsterite can be approximately treated with a single molar absorption coefficient.

4. Discussion

4.1. Clumped OH/F defects in natural olivine samples

The synthetic forsterite samples display a characteristic IR spectrum in the OH stretching-region that we confidently assign to the presence of clumped fluoride-hydroxyl defects. The reported spectra are similar to those of Fabbri et al. (2013) and can be observed also in various natural F-rich olivines from crustal environments (Sykes et al., 1994; Libowitzky and Beran, 1995) and in a kimberlite megacryst from Monastery mine with up to 47 ppm F (Bell et al., 2004; Mosenfelder et al., 2011, 2013a) and in some olivines from the Udachnaya kimberlite outcrop (Kishina et al., 2001; Matsyuk and Langer, 2004; Koch-Müller et al., 2006). The latter have not yet been analyzed for fluorine, but the presence of melt inclusions with F-rich phases suggests that some F may have been incorporated in the host olivines (Golovin et al., 2007). This indicates that the results of our experiments as well as those from Fabbri et al. (2013) are directly applicable to natural conditions. In particular, the Mg/(Mg+Fe) molar ratio, which varies from 86.00 to 99.65 in the natural samples discussed above (Sykes et al., 1994; Libowitzky and Beran, 1995) does not modify the IR OH stretching bands. This is also true for the kimberlitic olivines investigated by Bell et al. (2004) and Mosenfelder et al. (2011). The positions of their OH stretching bands are similar, within 5 cm⁻¹, to those reported in the present study for Fe-free samples. Consequently the incorporation mechanisms and solubility of fluorine are not expected to be significantly changed in presence of iron. The present results also indicate that some OH IR bands observed by Sykes et al. (1994) in a boron and fluorine rich olivine (0.33-0.55 wt% F and

0.35-0.40 wt% B) could be explained without having to consider F-B coupled substitutions. Additionally FTIR measurements prove to be useful for the identification of F-rich olivine including Fe-rich olivine. It must be noted however that this IR signature is not observed for synthetic hydrous olivines from Withers et al. (2011) and (2012) that contain up to 47 ppm F, despite not having been intentionally doped with fluorine (Table 1). On the other hand, the natural olivines ROM177 and GRR1012-2 containing 37 and 47 ppm F, respectively (Mosenfelder et al., 2013a), display the IR signature assigned here to clumped fluoride-hydroxyl defects. This apparent discrepancy might be explained by the ratio of the fluorine to water contents. With less than 220 ppm H₂O, the fluorine-related defects are still distinguishable by FTIR measurements, whereas in the synthetic olivines containing more water, the F-free hydroxyl defects are dominant.

Similar studies on other NAMs may reveal comparable processes, even though first studies on F-bearing pyroxenes (Mosenfelder and Rossman, 2013a and 2013b) have not revealed so far characteristic IR OH stretching bands that could be linked to incorporation of fluorine.

4.2. Cooperative solubility of water and fluorine in olivine

In nominally anhydrous silicates, the hydrolytic weakening mechanism consists in an increase of cationic vacancy concentration in presence of water due to a thermodynamic stabilization of the vacancies by the presence of the charge compensating protons (Brodholt and Refson, 2000). Our experimental and theoretical results indicate that mixed OH/F defects display an even greater stability. Therefore, the presence of fluoride ions should contribute to the hydrolytic weakening mechanism. An important consequence of this cooperative effect is that the dependence of water solubility in forsterite on water fugacity should be modified in presence of fluoride. Indeed, this dependence is a function of the number of OH groups

associated with a specific OH defect (Keppler and Bolfan-Casanova, 2006). In high pressure F-free forsterite samples, water incorporation is dominated by $(4\text{H})^{\text{x}}_{\text{Si}}$ defects and to a lesser proportion by interstitial defects (Ingrin et al., 2013). Thus, the replacement of $(4\text{H})^{\text{x}}_{\text{Si}}$ defects by clumped F/OH defects should lead to a decrease in the fugacity exponent between the F-free and F-bearing system.

4.3. Geodynamical implications

We show that fluorine solubility can reach more than 1300 ppm in hydrous olivine at pressures and temperatures relevant of the upper-mantle. Such high solubility implies that significant amounts of fluorine can be stored in nominally anhydrous minerals in the upper mantle.

Our experiments establish the link between F and OH assimilation in mineral networks. This must be particularly true in subduction settings where water is recycled back to the mantle. Indeed, if F and OH are associated, F could be recycled in the mantle together with water through F incorporation in NAMs in a peridotitic layer at the bottom of the down-going oceanic lithosphere. In that case fluorine could be transferred in deeper regions of subduction zones "en route" to the transition zone and lower mantle during deep hydrous mineral transformations in subducted slabs such as in the phase B (Hazen et al., 1997). Furthermore, recent results have demonstrated the capability of the transition zone to contain fluorine through an experimental study of the solubility of fluorine in ringwoodite and wadsleyite (Roberge et al., 2013).

To conclude, water and fluorine geodynamical cycles are likely to be strongly connected in the mantle owing to the existence of clumped defects in nominally anhydrous minerals.

Acknowledgements

We are grateful to Olivier Beyssac for access to the Raman spectrometer, to Benoit Baptiste for help in the sample preparation, to the CAMPARIS staff who provided help for microprobe analyses and to Guillaume Morard for his assistance. We thank the very efficient LEEL staff who helped us during PIGE session. The SEM facility of IMPMC is supported by Region Ile de France Grant SESAME 2006 NOI-07-593/R, INSU-CNRS, UPMC and ANR grant ANR-07-BLAN-0124-01. High-pressure experiments were supported by an ERC grant to C.S. (FP7 grant agreement no. 259649). The theoretical work was performed using HPC resources from GENCI-IDRIS (Grant 2013-i2013041519) and using the IBM iDataPlex cluster of the UPMC. We also thank J. Mosenfelder and an anonymous reviewer who helped us improving the manuscript.

References

- Aoki, K., Ishiwaka, K., Kanisawa, S., 1981. Fluorine Geochemistry of Basaltic Rocks from Continental and Oceanic Regions and Petrogenetic Application. *Contrib. Mineral. Petrol.* 76, 53-59.
- Balan, E., Refson, K., Blanchard, M., Delattre, S., Lazzeri, M., Ingrin, J., Mauri, F., Wright, K., Winkler, B., 2008. Theoretical infrared absorption coefficient of OH groups in minerals. *Am. Mineral.* 93, 950–953.
- Balan, E., Ingrin, J., Delattre, S., Kovacs, I., Blanchard, M., 2011. Theoretical infrared spectrum of OH-defects in forsterite. *Eur. J. Mineral.* 23, 285–292.
- Balan, E., Yi, H., Blanchard, M., 2013. First-principles study of OH defects in zircon. *Phys. Chem. Minerals* 40, 547–554.
- Balan, E., Blanchard, M., Lazzeri M., Ingrin, J., 2013. Contribution of interstitial OH groups to the incorporation of water in forsterite. *Phys. Chem. Minerals* DOI 10.1007/s00269-013-0628-y.
- Bali, E., Bolfan-Casanova, N., Koga K.T., 2008. Pressure and temperature dependence of H solubility in forsterite: An implication to water activity in the Earth interior. *Earth Planet. Sci. Lett.* 268, 354-363.
- Baroni, S., Giannozzi. P., 2001. Phonons and related properties of extended systems from Density-functionnal perturbation theory. *Rev. Mod. Phys.* 73, 515–562.
- Bell, D.R., Rossman, G.R., 1992. Water in Earth's Mantle: the role of Nominally Anhydrous Minerals. *Science* 255, 1391-1397.

443 Bell, D.R., Rossman, G.R., Moore, R.O., 2004. Abundance and Partitioning of OH in a High-
 444 pressure Magmatic System: Megacrysts from the Monastery Kimberlite, South Africa.
 445 J. Pet. 45, 1539-1564.

446 Beran, A., Libowitzky, E., 2006. Water in natural mantle minerals. II. Olivine, garnet and
 447 accessory minerals. Rev. Mineral. Geochem. 62, 169-191.

448 Bernini, D., Wiedenbeck, M., Dolejs, D., Keppler, H., 2013. Partitioning of halogens between
 449 mantle minerals and aqueous fluids: implications for the fluid flow regime in
 450 subduction zones. Contrib. Mineral. Petrol. 165, 117–128.

451 Berry, A.J., Hermann, J., O'Neill, H.S.C., Foran, G.J., 2005. Fingerprinting the water site in
 452 mantle olivine. Geology 33, 869-872.

453 Berry, A.J., O'Neill, H.St.C., Hermann, J., Scott, D.R., 2007. The infrared signature of water
 454 associated with trivalent cations in olivine. Earth Planet. Sci. Lett. 261, 134–142.

455 Beyer, C., Klemme S., Wiedenbeck, M., Stracke, A., Vollmer, C., 2012. Fluorine in
 456 nominally fluorine-free mantle minerals: Experimental partitioning of F between
 457 olivine, orthopyroxene and silicate melts with implications for magmatic processes.
 458 Earth Planet. Sci. Lett. 337-338, 1-9.

459 Borisov, A., Pack, A., Kropf, A., Palme, H., 2008. Partitioning of Na between olivine and
 460 melt: An experimental study with application to the formation of meteoritic Na₂O-rich
 461 chondrule glass and refractory forsterite grains. Geochim. Cosmochim. Acta 72,
 462 5558–5573.

463 Brey, G.P., Bulatov, V.K., Girnis, A.V., 2009. Influence of water and fluorine on melting of
 464 carbonated peridotite at 6 and 10 GPa. Lithos 112, 249–259.

465 Brodholt, J.P., Refson, K., 2000. An ab initio study of hydrogen in forsterite and a possible
 466 mechanism for hydrolytic weakening. *Journal of geophysical research* 105 B8, 18977-
 467 18982 .

468 Bromiley, D.W., Kohn, S.C., 2007. Comparisons between fluoride and hydroxide
 469 incorporation in nominally anhydrous and fluorine-free mantle minerals. *Goldschmidt*
 470 *Conference Abstracts* A124.

471 Bureau, H., Métrich, N., Pineau, F., Semet, P., 1998. Magma–conduit interaction at Piton de
 472 la Fournaise volcano (Réunion Island): a melt and fluid inclusion study. *J. Volcanol.*
 473 *Geotherm. Res.* 84, 39-60.

474 Bureau, H., Raepsaet, C., Khodja, H., Carraro, A.C., Aubaud, C., 2009. Determination of
 475 hydrogen content in geological samples using elastic recoil detection analysis
 476 (ERDA). *Geochim. Cosmochim. Acta* 73, 3311–3322.

477 Caruba, R., Baumer, A., Ganteaume, M., Iacconi, P., 1985. An experimental study of
 478 hydroxyl groups and water in synthetic and natural zircons: a model of the metamict
 479 state. *Am. Miner.* 70, 1224-1231.

480 Dalou, C., Koga, K.T., Shimizu, N., Boulon, J., Devidal, J.L., 2012. Experimental
 481 determination of F and Cl partitioning between lherzolite and basaltic melt. *Contrib.*
 482 *Mineral. Petrol.* 163, 591-609.

483 Daudin, L., Khodja, H., Gallien, J.P., 2003. Development of “position–charge–time” tagged
 484 spectrometry for ion beam microanalysis. *Nuclear Instruments and Methods in Physics*
 485 *Research B* 10, 153-158.

486 Fabbrizio, A., Stalder, R., Hametner, K., Günther, N., Marquardt, K., 2013. Experimental
 487 partitioning of halogens and other trace elements between olivine, pyroxenes,

488 amphibole and aqueous fluid at 2 GPa and 900–1,300 °C. *Contrib. Mineral. Petrol.*
 489 DOI 10.1007/s00410-013-0902-5.

490 Frost, D., 2008. The upper mantle and Transition zone. *Elements* 4, 171- 176.

491 Giannozzi, P., Baroni, S., Bonini, N., Calandra, M., Car, R., Cavazzoni, C., Ceresoli, D.,
 492 Chiarotti, G. L., Cococcioni, M., Dabo, I., Dal Corso, A., de Gironcoli, S., Fabris, S.,
 493 Fratesi, G., Gebauer, R., Gerstmann, U., Gougoussis, C., Kokalj, A., Lazzeri, M.,
 494 Martin-Samos, L., 2009. QUANTUM ESPRESSO: a modular and open-source
 495 software project for quantum simulations of materials. *J. Phys. Condens. Matter* 21,
 496 395502.

497 Golovin, A.V., Sharygin, V.V., and Pokhilenko, N.P., 2007. Melt Inclusions in Olivine
 498 Phenocrysts in Unaltered Kimberlites from the Udachnaya-East Pipe, Yakutia: Some
 499 Aspects of Kimberlite Magma Evolution during Late Crystallization Stages.
 500 *Petrologiya* 15, 178–195.

501 Habrioux, A., Surblé, S., Berger, P., Khodja, H., D’Affroux, A., Mailley, S., Gutel, T.,
 502 Patoux, S., 2012. Nuclear microanalysis of lithium dispersion in LiFePO₄ based
 503 cathode materials for Li-ion batteries. *Nuclear Instruments and Methods in Physics*
 504 *Research B* 290, 13-18.

505 Hazen, M., Yang, H., Prewitt, C.T., Gasparik, T., 1997. Crystal chemistry of superfluorous
 506 phase B (Mg₁₀Si₃O₁₄F₄): Implications for the role of fluorine in the mantle. *Am.*
 507 *Mineral.* 82, 647-650.

508 Hervig, R. L., Bell, D. R., 2005. Fluorine and Hydrogen in Mantle Megacrysts. *AGU Fall*
 509 *Meeting* pp. V41A-1426.

510 Ingrin, J., Liu, J., Depecker, C., Kohn, S.C., Balan, E., Grant, K.J., 2013. Low-temperature
 511 evolution of OH bands in synthetic forsterite, implication for the nature of H defects at
 512 high pressure. *Phys. Chem. Minerals* 40, 499-510.

513 John, T., Scambelluri, M., Frische, M., Barnes, J.D., Bach, W., 2011. Dehydration of
 514 subducting serpentinite: Implications for halogen mobility in subduction zones and the
 515 deep halogen cycle. *Earth Planet. Sci. Lett.* 308, 65-76.

516 Kawamoto, T., 2006. Hydrous phases and water transport in the subducting slab. *Reviews in*
 517 *Mineralogy and Geochemistry* 62, 273-289.

518 Keppler, H., Bolfan-Casanova, N., 2006. Thermodynamics of water solubility and
 519 partitioning. *Reviews in Mineralogy and Geochemistry* 62, 193-230.

520 Khodja, H., Berthoumieux, E., Daudin, L., Gallien, J-P., 2001. The Pierre Süe Laboratory
 521 nuclear microprobe as a multi-disciplinary analysis tool. *Nuclear Instruments and*
 522 *Methods in Physics Research B* 181, 83-86.

523 Kishina, N.P., Wirth, R., Andrut, M., Ukanov, A.V., 2001. Extrinsic and intrinsic mode of
 524 oxygen occurrence in natural olivines : a FTIR and TEM investigation. *Phys. Chem.*
 525 *Minerals* 28, 291-301.

526 Klemme, S., 2004. Evidence for fluoride melts in Earth's mantle formed by liquid
 527 immiscibility. *Geology* 32, 441-444.

528 Koch-Müller, M., Matsyuk, S.S., Rhede, D., Wirth, R., Kishina, N., 2006. Hydroxyl in mantle
 529 olivine xenocrysts from the Udachnaya kimberlite pipe. *Phys. Chem. Minerals* 33,
 530 276–287.

531 Lemaire, C., Kohn S.C., Brooker, R.A., 2004. The effect of silica activity on the incorporation
 532 mechanisms of water in synthetic forsterite: a polarised infrared spectroscopic study.
 533 Contrib. Mineral. Petrol. 147, 48-57.

534 Libowitzky, E., Beran, A., 1995. OH Defects in Forsterite. Phys. Chem. Minerals 22, 387-
 535 392.

536 Matsyuk, S.S., Langer, K., 2004. Hydroxyl in olivines from mantle xenoliths in kimberlites of
 537 the Siberian platform. Contrib. Mineral. Petrol. 147, 413-437.

538 Mayer, M., 1997. SIMNRA User's Guide. Report IPP 9/113, Max-Planck-Institut für
 539 Plasmaphysik, Garching, Germany.

540 McDonough, W.F., Sun, S.S., 1995. The composition of the Earth. Chem. geol. 120,223-253.

541 Métrich, M., Rutherford, M.J., 1991. Experimental study of chlorine behavior in hydrous
 542 silicic melts. Geochim. Cosmochim. Acta 56, 607-616.

543 Mosbah, M., Métrich, N., Massiot, P., 1991. PIGME fluorine determination using a nuclear
 544 microprobe with application to glass inclusions. Nuclear Instruments and Methods in
 545 Physics Research B58, 227-231.

546 Mosenfelder, J.L., Le Voyer, M., Rossman, G.R., Guan, Y., Bell, D.R., Asimow, P., Eiler, J.,
 547 2011. Analysis of hydrogen in olivine by SIMS: Evaluation of standards and protocol.
 548 Am. Mineral. 96, 1725–1741.

549 Mosenfelder, J.L., Rossman G.R., 2013a. Analysis of hydrogen and fluorine in pyroxenes: I
 550 Orthopyroxene. Am. Mineral. 98, 1026–1041.

551 Mosenfelder, J.L., Rossman, G.R., 2013b. Analysis of hydrogen and fluorine in pyroxenes: II
 552 Clinopyroxene. Am. Mineral. 98, 1042–1054.

553 Palme, H., Jones, A., 2003. Solar system abundances of the elements. Treatise on
 554 geochemistry 1, 41-61.

555 Paul, D.K., Buckley, F., Nixon, P.H., 1976. Fluorine and Geochemistry of Kimberlites. Chem.
 556 Geol. 17, 125-133.

557 Perdew, J.P., Burke, K., Ernzerhof, M., 1996. Generalized Gradient Approximation Made
 558 Simple. Phys. Rev. Lett. 77, 3865-3868.

559 Pyle, D.M., Mather, T.A., 2009. Halogens in igneous processes and their fluxes to the
 560 atmosphere and oceans from volcanic activity: A review. Chemical Geology 263, 110-
 561 121.

562 Raepsaet, C., Bureau, H., Khodja, H., Aubaud, C., Carraro, A., 2008. μ -ERDA developments
 563 in order to improve the water content determination in hydrous and nominally anhydrous
 564 mantle phases. Nuclear Instruments & Methods in Physics Research Section B-Beam
 565 Interactions with Materials and Atoms, 266: 1333-1337.

566 Roberge, M., Bureau H., Bolfan-Casanova, N., Frost, D.J., Raepsaet, C., Surblé, S., Khodja,
 567 H., Fiquet, G., 2013. F and Cl solubilities in wadsleyite and ringwoodite. Goldschmidt
 568 Conference, Florence, August 26-31, Italy.

569 Robert, J.L., Della Ventura, G., Hawthorne, H.C., 1999. Near-infrared study of short-range
 570 disorder of OH and F in monoclinic amphiboles. Am. Mineral. 84, 86-91.

571 Schilling, J.G., Bergeron, M.B., Evans, R., 1980. Halogens in the mantle beneath the North
 572 Atlantic. Phil. Trans. R. Soc. Lond. A 29, 147-178.

573 Smith, J.V., Delaney, J.S., Hervig, R.L., Dawson, J.B., 1981. Storage of F and Cl in the upper
 574 mantle: geochemical implications. Lithos 14, 133-147.

575 Smith, J.V., 1981. Halogen and Phosphorous storage in the Earth. *Nature* 289, 762-765.

576 Straub, S.M., Layn, G.D., 2003. The systematics of chlorine, fluorine, and water in Izu arc
577 front volcanic rocks: Implications for volatile recycling in subduction zones. *Geochim.*
578 *Cosmochim. Acta* 67, 4179–4203.

579 Sykes, D., Rossman, G., Veblen, D., Grew, E., 1994. Enhanced H and F incorporation in
580 borian olivine. *Am. Mineral.* 79, 904-908.

581 Symonds, R.B., Rose, W.I., Reed, M.H., 1988. Contribution of Cl and F bearing gases to the
582 atmosphere by volcanoes. *Letters to Nature* 334, 415-418.

583 Umemoto, K., Wentzcovitch, R.M., Hirschmann, M.M., Kholstedt, D., Withers, A., 2011. A
584 first-principles investigation of hydrous defects and IR frequencies in forsterite: The case
585 for Si vacancies. *Am. Mineral.* 96, 1475-1479.

586 Visser, D., 1993. Fluorine-bearing Hydrogarnets from Blengsvatn, Bamble Sector, South
587 Norway. *Mineralogy and Petrology* 47, 209-218.

588 Withers, A.C., Hirschmann, M.M., Tenner, T.J., 2011. The effect of Fe on olivine H₂O
589 storage capacity: Consequences for H₂O in the martian mantle. *Am. Mineral.* 96,
590 1039-1053

591 Withers, A.C., Bureau H., Raepsaet, C., Hirschmann, M.M., 2012. Calibration of infrared
592 spectroscopy by elastic recoil detection analysis of H in synthetic olivine. *Chem. Geol.*
593 334, 92-98.

594 Withers, A.C, 2013. On the use of unpolarized infrared spectroscopy for quantitative analysis
595 of absorbing species in birefringent crystals. *Am. Mineral.* 98, 689-697.

596

Table 1

Synthesis conditions, chemical compositions of forsterite samples and positions of the observed absorption bands with their corresponding area and width. Infrared band position, area and full width at half height (FWHH) from fit of the spectra by Lorentzian functions (see text). Detailed polarized IR measurements of samples A710 and M475 are to be found in Withers et al. (2011).

NAME	Mg # ¹	P-T	F (ppm) ²	H ₂ O (ppm) ³	Na (ppm) ²	Band position (cm ⁻¹)	Area (cm ⁻²)	FWHH (cm ⁻¹)
PC36F	100 Mg _{2.02} Si _{0.99} O ₄	2 GPa 1230- 1260°C	1715 (±172) det. lim. = 12	887 (±124)	131(±13) det. lim. = 28	3674.3*	180.78	5.43
						3641.0*	407.08	8.12
						3624.3*	47.27	3.88
						3612.0	10.00	5.00
						3597.1	160.32	7.42
						3591.5	175.51	6.23
						3569.9*	848.61	10.75
						3555.1	27.08	4.08
						3535.1*	277.22	5.62
						3514.7*	47.16	3.76
						3480.7, 3218.2, 3040.0	13.64, 21.5, 27.88	34.50, 36.50, 30.00
PC38F	100 Mg _{1.99} Si _{1.01} O ₄	4 GPa 1240- 1255°C	1308 (±131) det. lim. = 10	267 (±53)	81(±8) det. lim. = 6	3674.4*	38.92	4.57
						3640.8*	200.30	7.68
						3624.2*	45.74	4.74
						3613.1	10.00	5.00
						3597.9	50.79	5.46
						3591.5	158.15	7.73
						3569.9*	516.02	10.36
						3555.0	53.18	6.14
						3536.2*	117.02	6.71
						3514.0*	10.00	5.00
						3480.2, 3347.8, 3322.1, 3212, 3161.0	4.73, 4.89, 1.16, 15, 105	9.76, 9.35, 5.25, 40, 43.78

NAME	Mg # ¹	P - T	F (ppm) ²	H ₂ O (ppm) ³	Na (ppm) ²	Band position (cm ⁻¹)	Area (cm ⁻²)	FWHH (cm ⁻¹)
PC38	100 Mg _{1.97} Si _{1.01} O ₄	4 GPa 1240- 1255°C	< 13 det. lim. = 13	448 (±90)	< 14 det. lim. = 14	3612.5	58.09	6.58
						3598.8 [†]	50.10	17.15
						3591.0	18.00	9.02
						3579.1	38.20	9.23
						3566.8	28.27	9.42
						3550.6 [†]	12.56	18.35
						3528.4	42.32	32.31
						3480.7, 3446.7, 3418.0, 3404.0 3388.0, 3347.0, 3321.5, 3303.0 3279.0, 3217.0, 3157.6, 3038.0	20.1, 10.73, 0.19, 5.69, 1.22, 10.73, 6.70, 0.50, 0.10, 17.34, 39.25, 8.28	17.29, 13.43, 3.74, 7.93, 8.45, 13.43, 11.49, 10.00, 3.00, 3.01, 47.24, 31.00
A710	90.2	3 GPa 1250°C	46 (±5) det. lim. = 5	468 (±81)	< 15 det. lim. = 15	3613		
						3597 [†]		
						3577		
						3567		
						3538		
						3500, 3477, 3450, 3302		
M475	90.3	10 GPa 1250°C	47 (±5) det. lim. = 12	2019 (±332)	< 25 det. lim. = 25	3611		
						3597 [†]		
						3580		
						3567		
						3550 [†]		
						3475, 3447		

- 2 ¹ determined by EPMA, ² by PIGE and ³ by ERDA. For IR absorption bands, *indicates F-related bands and [†] possible bands related to OH-
- 3 interstitials.

Figure 1:

Secondary electron image of forsterite grains (synthesis #PC36F)

Figure 2:

Unpolarized average infrared spectra of synthetic forsterite (black dots) and fit of spectra by a sum of Lorentzian functions in grey line (see parameters of the Lorentzian functions in Table 1). Lowermost spectrum absorbance is multiplied by a factor of 4 and spectra are offset vertically for clarity.

Figure 3:

Unpolarized infrared spectra of forsterite grains derived from the synthesis #PC38F.

Figure 4:

a) Structural models of the most stable configurations for OH/F substitutions in Si vacancy investigated by first-principles calculations. In $3F_{(O3, O3, O2)}$, the OH group points toward the center of the vacancy. In $2F_{(O2, O1)}$ the two OH groups point toward the F in O1 site. In $2F_{(O2, O3)}$ the OH in O1 site points toward the F in O3 site while the OH in O3 site points toward O in O1 site. In $F_{(O1)}$ all OH groups are pointing toward the F atom. In $F_{(O2)}$ the OH in O1 site points toward the F while the two OH in O3 sites point toward the O1 atom. In $F_{(O3)}$ the OH in O1 site points toward the F while the other two OH point toward O in O1 site. Theoretical polarized IR spectra for one (b), two (c) and three (d) OH/F substitutions. Red vertical lines correspond to the position of the OH bands in the fully protonated Si vacancy (Balan et al., 2011). The integrated molar absorption coefficient of the corresponding OH defects is indicated in the figure's legend (in cm^{-2} per mol $\text{H}_2\text{O/L}$).

Figure 5:

a) Polarized IR spectra of Pamir olivine from Libowitzky and Beran (1995) compared to the unpolarized average IR spectrum of run #PC38F. a.b. indicates the absence of the broad shoulder observed in F-rich forsterite samples at $\sim 3555\text{ cm}^{-1}$.

b) Calculated polarized spectra considering one, two and three OH/F substitutions in the Si vacancy. Proportions of the various configurations were taken into account following Umemoto et al. (2011) though variation in energy is too weak to induce major changes of relative intensities.

Figure 6:

Theoretical integrated molar absorption coefficients for the different F- and OH-bearing defects. The solid line corresponds to the theoretical correlation obtained by Balan et al. (2010), dashed line is a guide for the eyes.

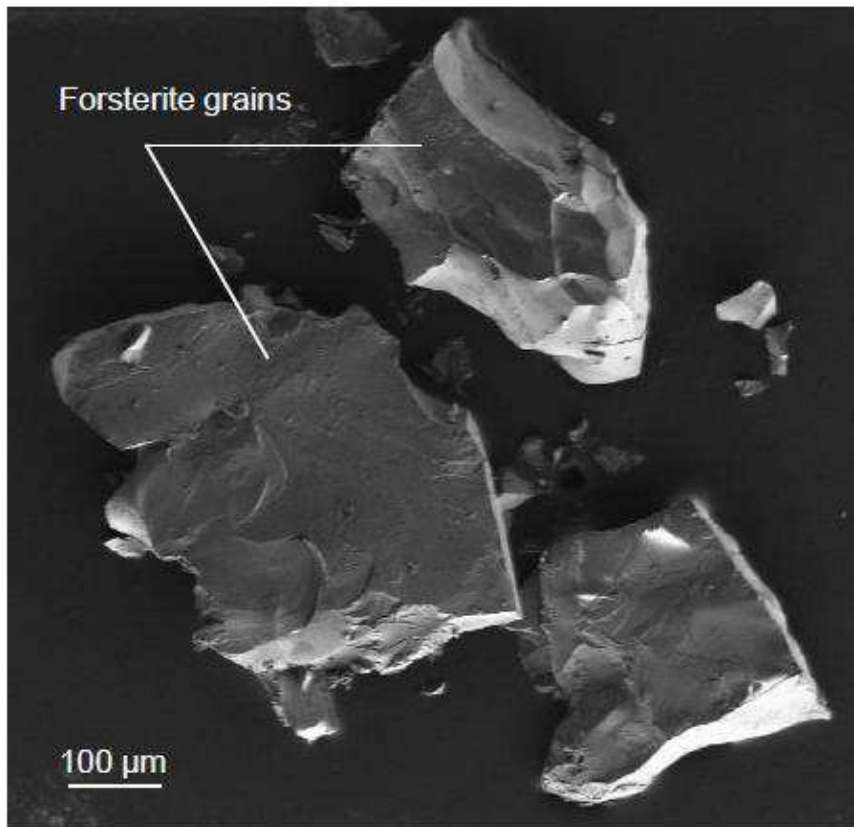
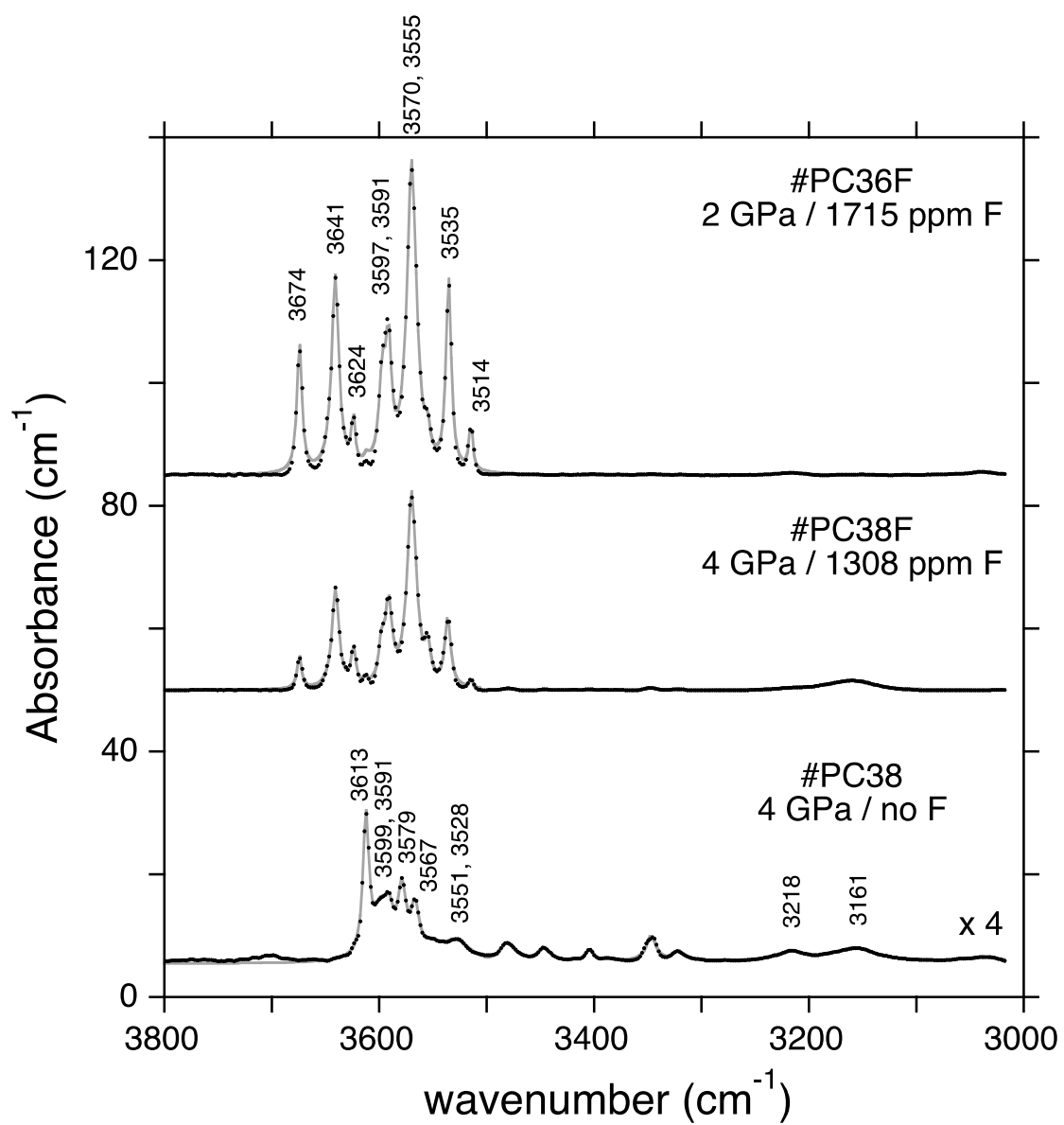


Fig. 1.



46 **Fig. 2.**

47

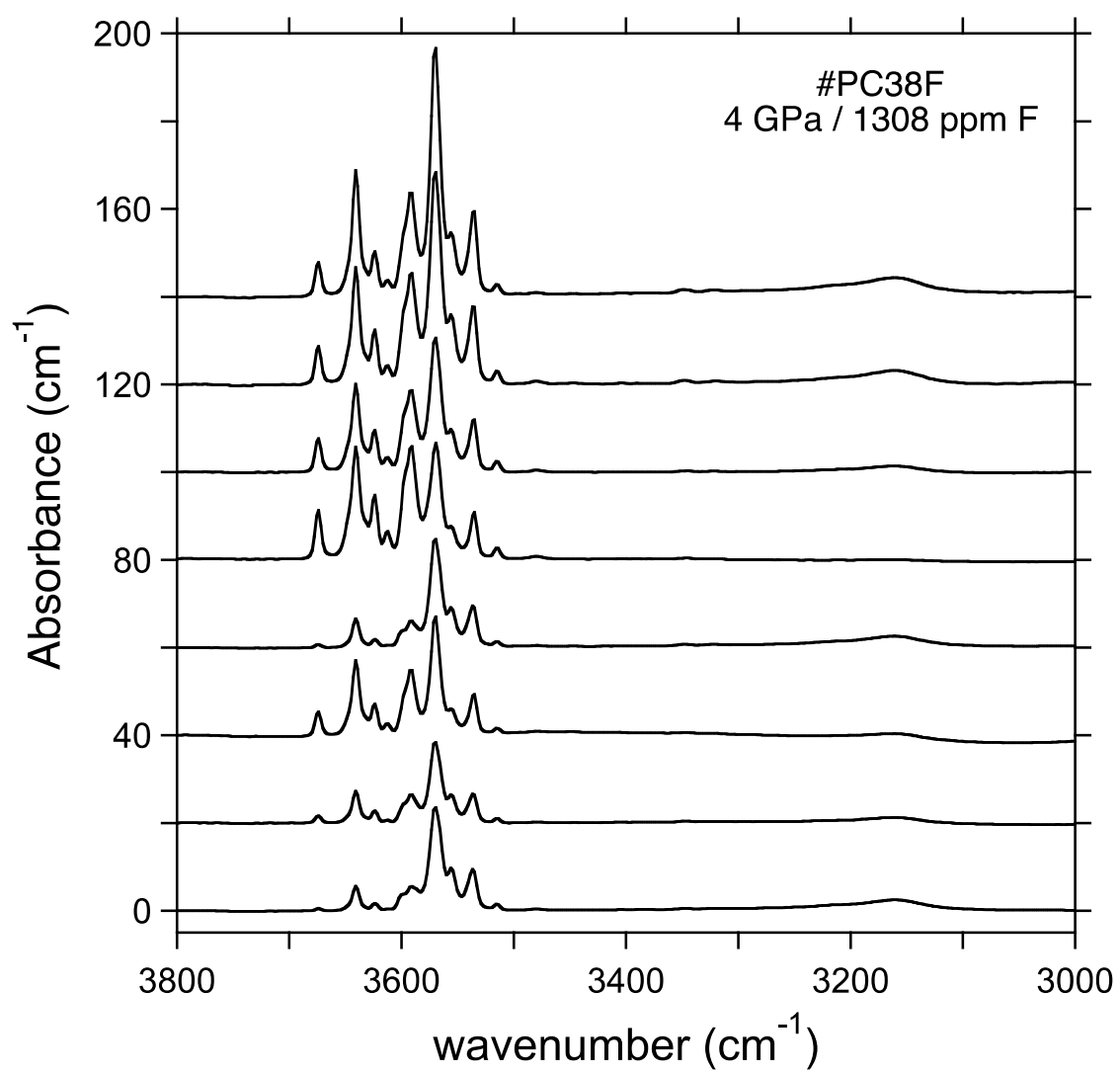


Fig. 3.

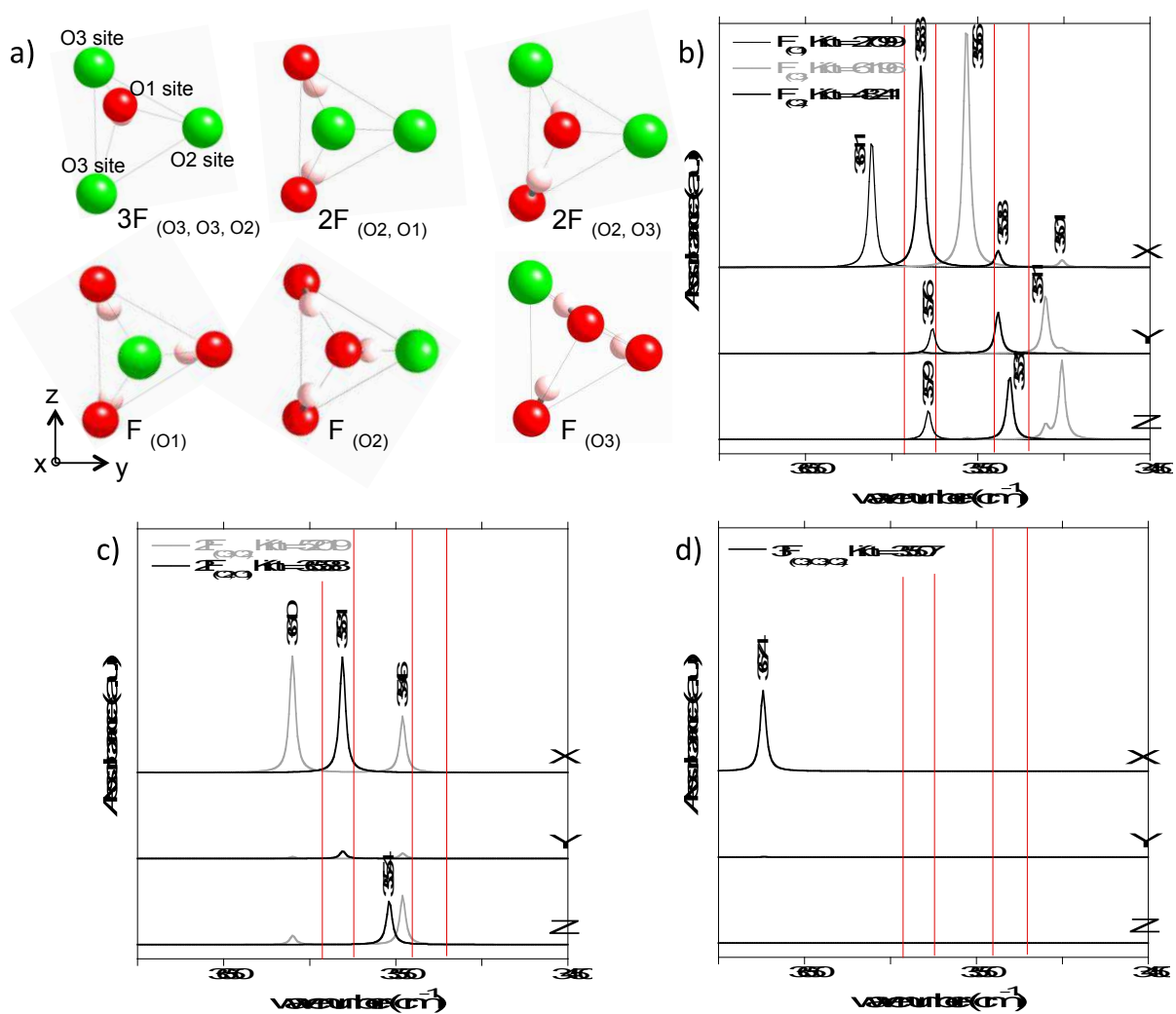


Fig. 4.

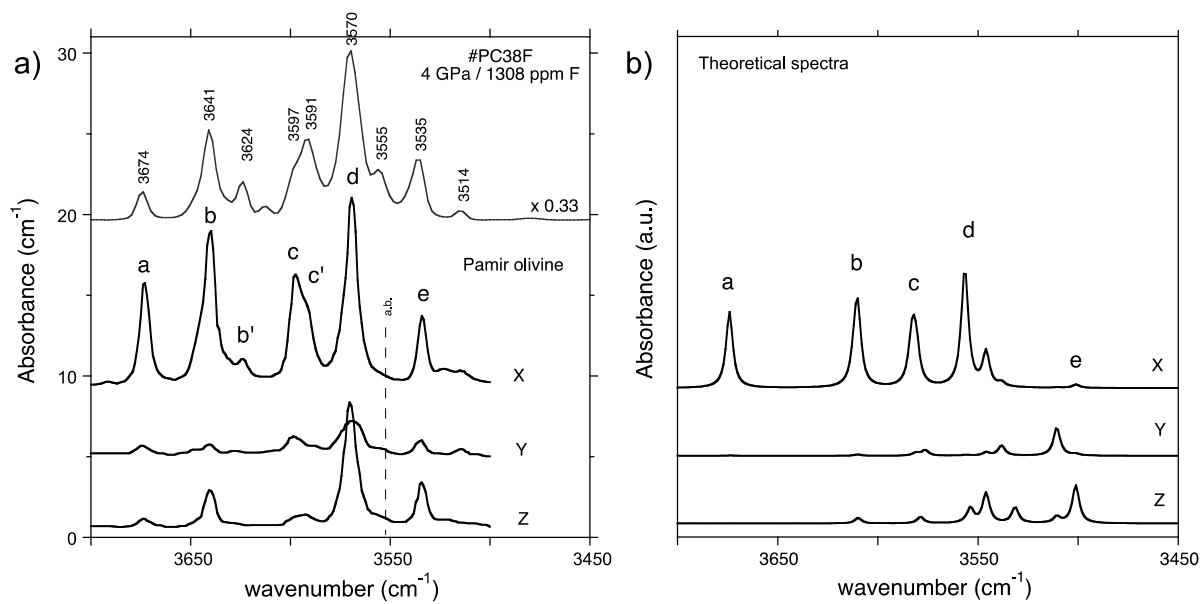


Fig. 5.

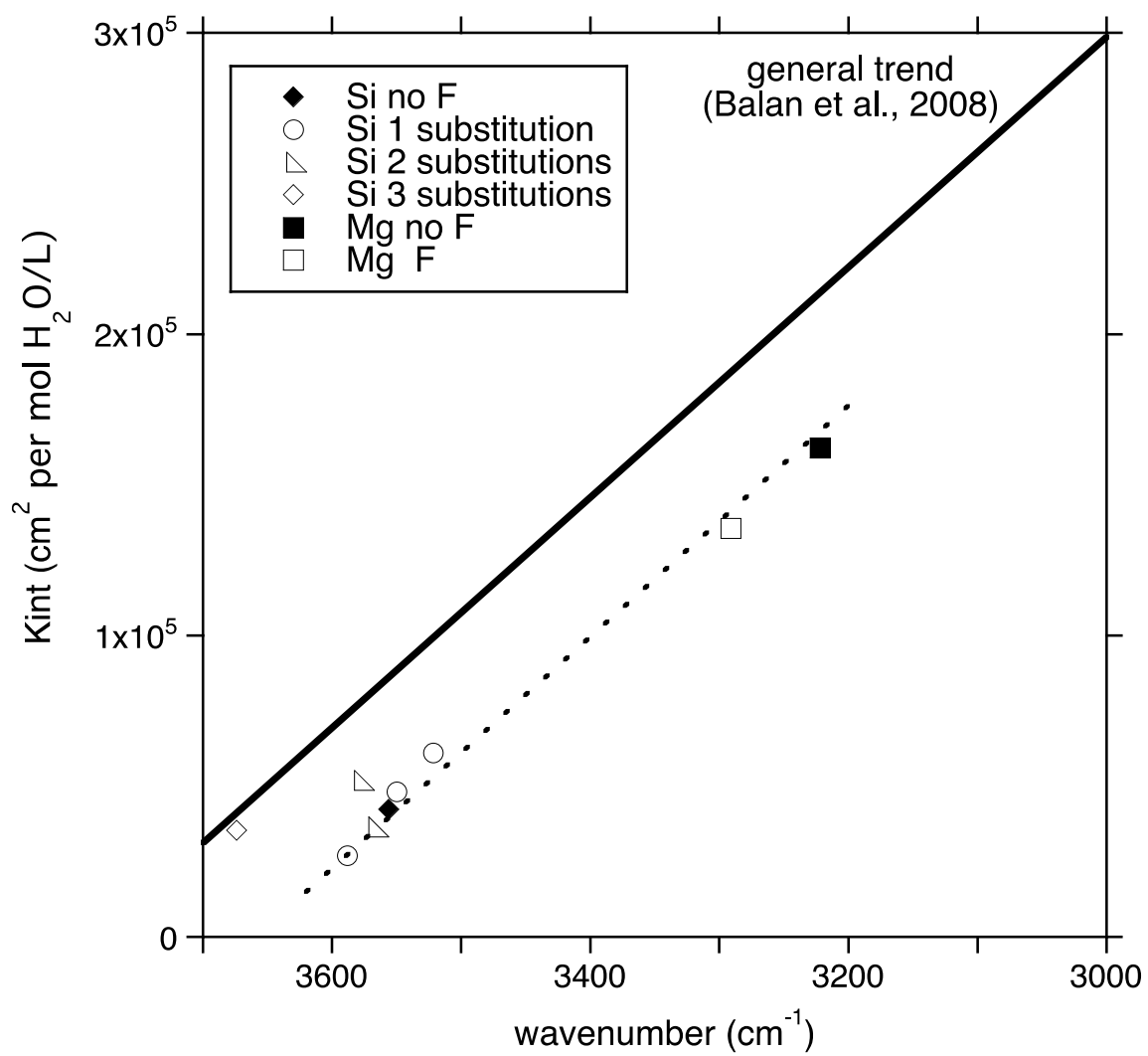


Fig. 6.